Dalton Transactions

ROYAL SOCIETY OF CHEMISTRY

PAPER

View Article Online
View Journal | View Issue

Cite this: *Dalton Trans.*, 2025, **54**, 16363

Design of a 1532 nm-driven red upconverter with high color purity for optical thermometry and anti-counterfeiting applications

Guotao Xiang, *[a,b] Hongdou Chen,[a] Yuanyuan Yi,[a] Zhiyu Yang,[a] Yongjie Wang,[a] Lu Yao,*[a] Xianju Zhou,[a] Li Li,[a] Xiaojun Wang[d] and Jiahua Zhang *[c]

The development of high color purity red upconversion (UC) materials operating within the second near-infrared (NIR) biological window (NIR-II) holds significant research importance for enhancing the penetration depth of such materials in biological tissues. Herein, near-pure red UC luminescence excited by a 1532 nm wavelength is achieved in $CaSc_2O_4$:Er^{3+} through Ho^{3+} doping, showing an approximately 19-fold improvement in the red-to-green emission ratio. Such a huge improvement in emission color purity results from the effective modulation of energy transfer (ET) mechanisms by Ho^{3+} ions, which is fully evidenced by the steady state and transient spectroscopic data. Utilizing the Stark splitting of Er^{3+}:$^4F_{9/2} \rightarrow {}^4I_{15/2}$ and Er^{3+}:$^4I_{11/2} \rightarrow {}^4I_{15/2}$ transitions, highly sensitive optical temperature sensing is realized with detection depths in biological tissues of about 6 mm and 8 mm, respectively. Furthermore, $CaSc_2O_4$:Er^{3+}/Ho^{3+} exhibits different luminescence colors under the excitation of 980 nm and 1532 nm wavelengths, enabling its optical anti-counterfeiting application with high concealment and security. These findings present a novel strategy to design NIR II-responsive red UC materials with high color purity for biomedicine and anti-counterfeiting applications.

Received 19th August 2025,
Accepted 8th October 2025

DOI: 10.1039/d5dt01973g

rsc.li/dalton

Introduction

Rare earth ion-doped upconversion (UC) luminescent materials can convert low-energy photons into high-energy photons for emission, a unique optical property that enables their extensive applications spanning from life sciences to information technology.[1–3] Under the excitation of near-infrared (NIR) light, the ultraviolet and visible light emitted by these materials holds significant application potential in non-contact optical thermometry, biological imaging, optical anti-counterfeiting, three-dimensional displays and other fields, benefiting from their desirable characteristics including long fluorescence lifetime, narrow emission bandwidth, low cytotoxicity and superior photostability.[4–6] Nevertheless, conventional UC materials predominantly utilize Yb^{3+} and Nd^{3+} as sensitizers with the excitation wavelengths of 980 nm and 808 nm, respectively, both falling within the first NIR biological window (NIR-I, 650 nm–1000 nm), which somewhat restricts their penetration depth in biological tissues, thereby making it challenging to meet the demands of clinical applications.[7–11]

Recently, several studies have indicated that Er^{3+} can achieve robust UC emission through a self-sensitization mechanism under the excitation of around 1532 nm wavelength, corresponding to the Er^{3+}:$^4I_{13/2}$ state.[12–14] For instance, Sun *et al.* observed intense green and red UC emissions in $NaErF_4$@$NaYF_4$ nanoparticles with an excitation wavelength of 1550 nm.[15] Meanwhile, Yin *et al.* reported the realization of underwater communication and narrowband NIR photodetection using a 1532 nm-driven $NaYS_2$:Er^{3+} phosphor.[16] More importantly, the 1532 nm wavelength falls within the second NIR biological window (NIR-II, 1000 nm–1700 nm), where biological tissues exhibit extremely weak absorption and scattering effects for light in this range, making these materials promising candidates for applications in deep biological tissues.[17–20]

Despite the advantages mentioned above, the complex energy landscape of Er^{3+}, characterized by multiple metastable energy levels, results in multicolor UC luminescence.[21–24] Such

[a]*Chongqing Key Laboratory of Dedicated Quantum Computing and Quantum Artificial Intelligence, School of Electronic Science and Engineering, Chongqing University of Posts and Telecommunications, 2 Chongwen Road, Chongqing 400065, China. E-mail: xianggt@cqupt.edu.cn, yaolu@cqupt.edu.cn*
[b]*Key Laboratory of Big Data Intelligent Computing, Chongqing University of Posts and Telecommunications, 2 Chongwen Road, Chongqing 400065, China*
[c]*State Key Laboratory of Luminescence and Applications, Changchun Institute of Optics, Fine Mechanics and Physics, Chinese Academy of Sciences, 3888 Eastern South Lake Road, Changchun 130033, China. E-mail: zhangjh@ciomp.ac.cn*
[d]*Department of Physics & Astronomy, Georgia Southern University, Statesboro, Georgia 30460, USA*

spectral diversity presents significant challenges for quantitative cellular imaging, biological tissue labeling applications, and so on.[25–28] Therefore, it is of great significance to develop effective strategies to achieve intense UC luminescence with high color purity driven by 1532 nm excitation in Er^{3+} self-sensitized UC materials, especially for red UC emission, which is conveniently located in the NIR-I region.[29–32]

In this work, the energy transfer (ET) pathways in $CaSc_2O_4$:Er^{3+} under the excitation of a 1532 nm wavelength are effectively modulated through Ho^{3+} doping, resulting in strong red UC emission with exceptionally high color purity. The underlying ET mechanism governing this optimized UC performance is elucidated in detail based on the spectral data. Furthermore, the optical thermometry and fluorescence anti-counterfeiting capabilities along with the penetration depth in the biological tissues of $CaSc_2O_4$:Er^{3+}/Ho^{3+} are thoroughly investigated. All data indicate that the obtained phosphor is an efficient red UC luminescent material that not only enables highly sensitive optical temperature monitoring in deep biological tissues but also provides fluorescence anti-counterfeiting ability with excellent covertness.

Experimental section

Chemicals

$CaCO_3$ (99.99%), Sc_2O_3 (99.99%), Ho_2O_3 (99.99%) and Er_2O_3 (99.99%) were supplied by Shanghai Aladdin Biochemical Technology Co., Ltd. All chemical reagents were used as raw materials without further purification.

Preparation

A traditional high-temperature solid-state reaction is used to synthesize $CaSc_2O_4$:15% Er^{3+}/x% Ho^{3+} (x = 0, 0.1, 0.5, 1, 2, 5) phosphors. First, oxide powders precisely weighed according to the stoichiometric ratio are thoroughly mixed *via* a grinding process in an agate mortar for 45 minutes. Subsequently, the resultant powder mixture is transferred to an alumina crucible and subjected to a presintering treatment in a box furnace at 600 °C for 3 hours. After cooling to the ambient temperature, the powders are ground again, followed by a final calcination in the same box furnace at 1400 °C for 6 hours under an air atmosphere to achieve the target sample.

Characterization

Powder X-ray diffraction (XRD) data are collected using a Persee XD-2 diffractometer. Spectroscopic data are measured using an Edinburgh Instruments FLS1000 spectrometer equipped with 980 nm and 1532 nm lasers as the excitation sources. The detector sensitivity of the FLS1000 spectrometer is greater than 35 000 : 1, estimated by the root mean square method. The 1532 nm laser exhibits a power stability of 0.240% operating for four continuous hours. During the spectral collection process, the sample temperature is controlled using an HFS600E-PB2 temperature control device supplied by Scientific Instruments.

Results and discussion

Structure and luminescence properties

The XRD patterns of the samples are tested to verify the crystal structures and phase purity. As illustrated in Fig. 1(a), the positions and relative intensities of the diffraction peaks for all samples exhibit excellent consistency with the standard card of $CaSc_2O_4$ (PDF#20-0234). No additional impurity phase is detected. However, a gradual shift of the XRD diffraction peaks toward lower angles is observed with the increasing Ho^{3+} concentration, which is attributed to the lattice expansion resulting from the substitution of Sc^{3+} ions (0.745 Å) by larger-radius Ho^{3+} ions (0.901 Å), according to Bragg's Law.

Fig. 1(b) presents the UC emission spectra of the samples doped with varying Ho^{3+} concentrations under the excitation of a 1532 nm wavelength, normalized at 551 nm. Four distinct emission bands are observed within the range of 500 nm to 900 nm, corresponding to the following Er^{3+} transitions: $^2H_{11/2} \rightarrow {}^4I_{15/2}$ peaked at 527 nm, $^4S_{3/2} \rightarrow {}^4I_{15/2}$ peaked at 551 nm, $^4F_{9/2} \rightarrow {}^4I_{15/2}$ peaked at 666 nm and $^4I_{9/2} \rightarrow {}^4I_{15/2}$ peaked at 798 nm. While the overall luminescence intensity decreases with the increasing Ho^{3+} concentration, the emission intensity ratio of red light ($^4F_{9/2} \rightarrow {}^4I_{15/2}$) to green light ($^2H_{11/2}$/$^4S_{3/2} \rightarrow {}^4I_{15/2}$) exhibits a significant improvement. As shown in Fig. 1(c), the red-to-green ratio reaches a maximum value of 77.0 at a Ho^{3+} concentration of 1%, which is approximately 19 times higher than that of the sample without Ho^{3+} doping. The corresponding CIE chromaticity diagram is presented in Fig. S1.

The dependence of UC luminescence intensity (I) on excitation power density (P) is subsequently investigated for $CaSc_2O_4$:Er^{3+}/Ho^{3+}. Generally speaking, the relationship between I and P in the UC luminescence processes follows

$$I \propto P^n. \quad (1)$$

Here, n represents the number of low energy photons absorbed to emit one high energy photon, which can be determined from the slope of the log(I)–log(P) curve. As depicted in Fig. 1(d), the n values for $^2H_{11/2} \rightarrow {}^4I_{15/2}$, $^4S_{3/2} \rightarrow {}^4I_{15/2}$ and $^4F_{9/2} \rightarrow {}^4I_{15/2}$ transitions are determined to be 2.9, 3.0 and 2.4, respectively, indicating that all three transitions are three-photon UC processes. In contrast, the n value of the $^4I_{9/2} \rightarrow {}^4I_{15/2}$ transition is 1.6, suggesting a two-photon UC process.

Based on the above analysis, the ET pathways within the samples can be deduced, as illustrated in Fig. 1(e). Under the excitation of a 1532 nm wavelength, Er^{3+} ions at the ground state undergo a ground state absorption (GSA) to be populated to the $^4I_{13/2}$ level. Subsequently, Er^{3+} ions at the $^4I_{13/2}$ state can be pumped to the $^4I_{9/2}$ state through an excited state absorption (ESA) process, followed by non-radiative relaxation and a second ESA process to realize the population of the red emitting $^4F_{9/2}$ level. Meanwhile, Er^{3+} ions at the $^4I_{9/2}$ level can absorb an additional 1532 nm photon, thereby being popu-

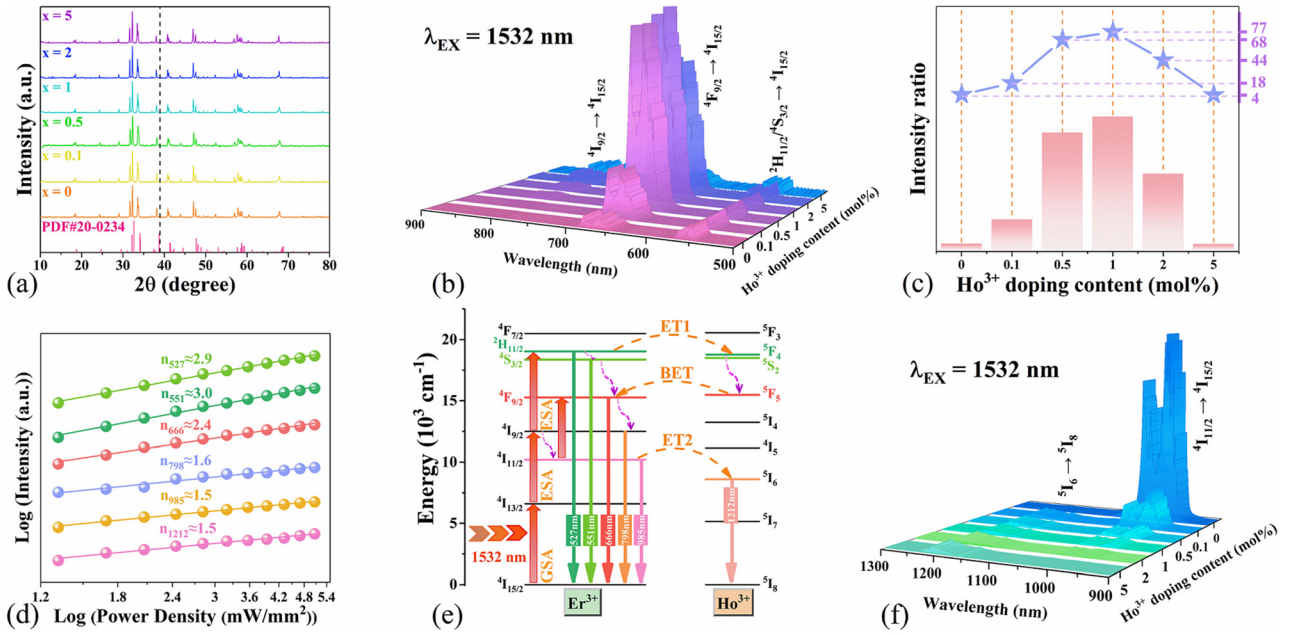

Fig. 1 (a) XRD patterns, (b) UC spectra and (c) intensity ratio of red to green emission of $CaSc_2O_4$:15% Er^{3+}/*x*% Ho^{3+} (*x* = 0, 0.1, 0.5, 1, 2, 5) with an excitation power density of about 1.35 mW mm^{-2}. (d) Power density dependence of emission intensity and (e) possible ET mechanism in the sample. (f) NIR spectra of $CaSc_2O_4$:15% Er^{3+}/*x*% Ho^{3+} (*x* = 0, 0.1, 0.5, 1, 2, 5).

lated to the green emitting $^2H_{11/2}/^4S_{3/2}$ levels. When Ho^{3+} ions are incorporated into the sample, efficient ET processes occur between Er^{3+} and Ho^{3+}. On one hand, Er^{3+} at the $^2H_{11/2}/^4S_{3/2}$ levels can transfer energy to Ho^{3+} at the ground state through the ET1 process, promoting Ho^{3+} to its $^5F_4/^5S_2$ levels. Subsequent non-radiative relaxation of Ho^{3+} to the $^5F_5$ level enables energy back transfer (BET) to Er^{3+}, realizing the population of the $^4F_{9/2}$ level. On the other hand, Er^{3+} at the $^4I_{11/2}$ level can transfer energy to Ho^{3+} *via* the ET2 process, allowing the Ho^{3+} to be populated at its $^5I_6$ level and emit 1212 nm NIR light. The above two ET mechanisms significantly improve the red-to-green ratio and color purity of the samples.

To further validate the ET processes between Er^{3+} and Ho^{3+}, the NIR emission spectra of the samples with different Ho^{3+} concentrations are measured under the excitation of a 1532 nm wavelength. As shown in Fig. 1(f), the emission intensity of the Er^{3+}:$^4I_{11/2} \rightarrow {}^4I_{15/2}$ transition decreases significantly with increasing Ho^{3+} concentration, while the luminescence intensity of the Ho^{3+}:$^5I_6 \rightarrow {}^5I_8$ transition exhibits a gradual increase. Furthermore, as depicted in Fig. 2, the lifetime of the Er^{3+}:$^4I_{11/2}$ level decreases monotonically with the increase of Ho^{3+} doping concentration. These observations collectively confirm the occurrence of efficient ET processes from the Er^{3+}:$^4I_{11/2}$ to the Ho^{3+}:$^5I_6$ level. The ET efficiency η_{ET} from the Er^{3+}:$^4I_{11/2}$ to the Ho^{3+}:$^5I_6$ level can be calculated through the following formula:

$$\eta_{ET} = 1 - \tau_x/\tau_0, \quad (2)$$

where τ_0 represents the intrinsic fluorescence lifetime of the donor in the absence of the acceptor, and τ_x denotes the measured lifetime of the donor in the codoped system. Based on the lifetime data presented in Fig. 2, the ET efficiency is calculated to be 72.3% for $CaSc_2O_4$:15% Er^{3+}/1% Ho^{3+}.

Optical thermometry behaviors

Fig. 3(a) displays the red UC spectra of the sample measured at different temperatures, which are normalized at 682 nm. Several Stark splittings induced by the crystal field effect can be clearly observed. Notably, the relative intensities of these Stark sublevels exhibit a regular variation with increasing temperature. In fact, these Stark sublevels are thermally coupled due to their small energy spacing (ΔE), of which the fluorescence intensity ratio (FIR) follows the Boltzmann distribution:

$$FIR = I_{up}/I_{low} = B \cdot \exp(-\Delta E/k_B T). \quad (3)$$

Here, I_{up} and I_{low} represent the emission intensities of the upper and lower energy levels, respectively, B is a temperature-independent constant, k_B denotes the Boltzmann constant and T is the absolute temperature. In this case, the Stark splittings at 655 nm and 682 nm are selected for investigation. According to eqn (3), the relationship between FIR_R and temperature is derived as

$$FIR_R = I_{655}/I_{682} = 2.3 \cdot \exp(-428/T), \quad (4)$$

of which the corresponding fitting curve is illustrated in Fig. 3(b). The ΔE value between the two Stark sublevels is determined to be 298 cm^{-1} based on the fitting curve. As criti-

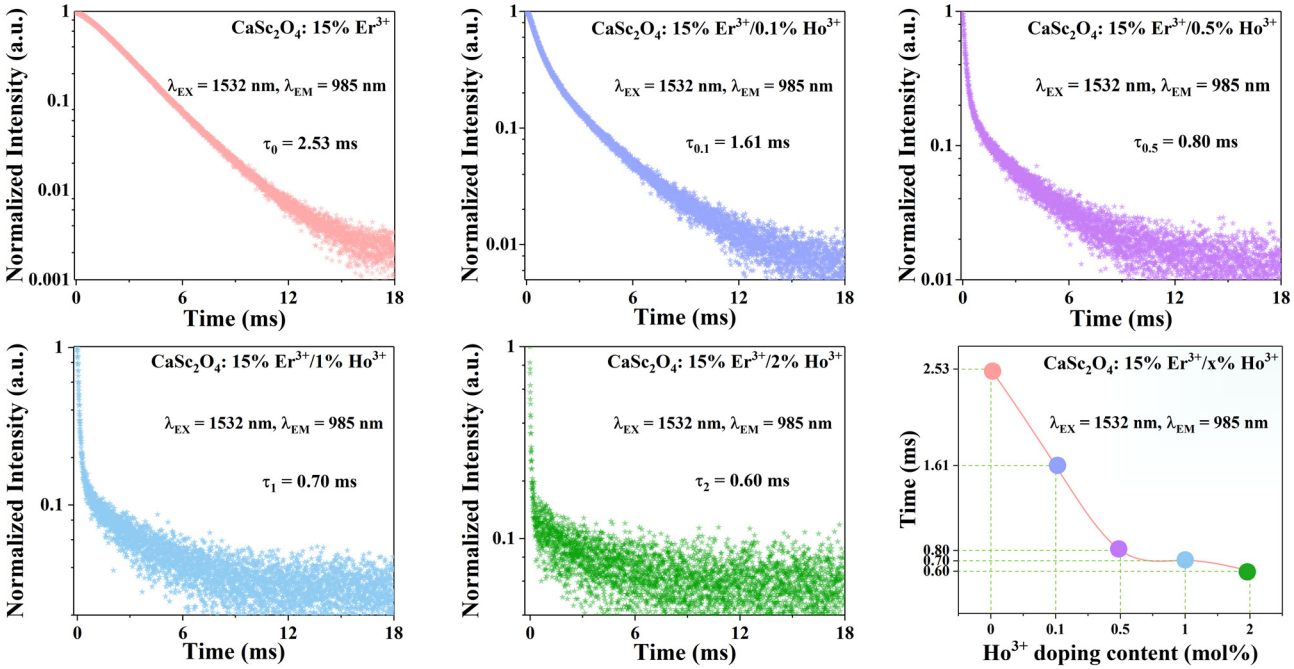

Fig. 2 Decay curves of the Er^{3+}:$^4I_{11/2}$ level in the samples with various Ho^{3+} doping concentrations along with the plot of lifetime values calculated by integrating the area under the corresponding decay curves with normalized initial intensity.

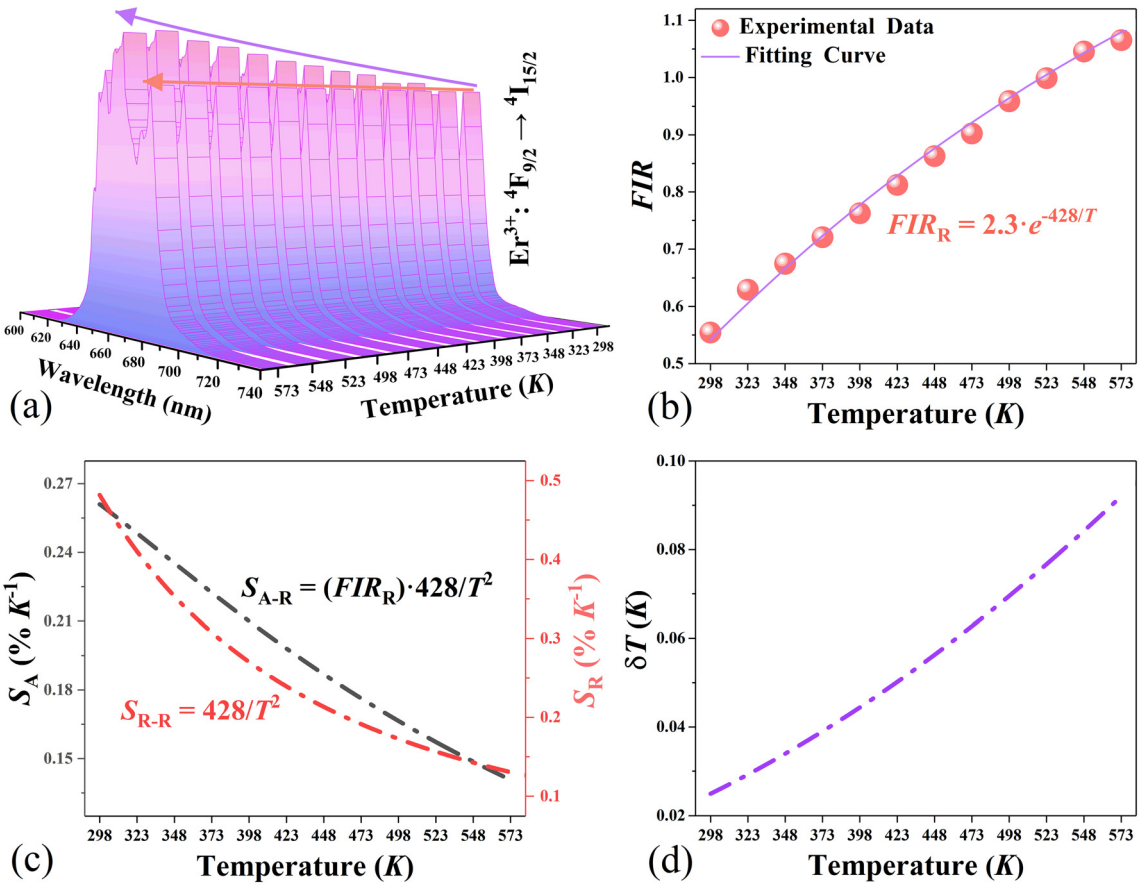

Fig. 3 Temperature dependence of (a) red UC emission along with the corresponding (b) FIR, (c) S_A and S_R and (d) δT.

cal parameters for evaluating optical thermometers, the absolute sensitivity (S_A) and relative sensitivity (S_R) can be calculated using the following equations:

$$S_A = |d(FIR)/dT|, \quad (5)$$

$$S_R = |d(FIR)/(FIR) \cdot dT|. \quad (6)$$

The fitted curves for S_A and S_R of the FIR_R-based optical thermometer are presented in Fig. 3(c), both exhibiting a decreasing trend with increasing temperature. The maximum values of S_A and S_R reach 0.26% K^{-1} and 0.48% K^{-1}, respectively, at the initial temperature. Temperature resolution (δT), another vital parameter for optical thermometers, is determined using

$$\delta T = (\delta FIR/FIR) \cdot (1/S_R), \quad (7)$$

where δFIR/FIR represents the relative uncertainty of FIR, primarily governed by the precision of the spectroscopic measurement equipment. As shown in Fig. S2(a), the δFIR/FIR value obtained from 50 repeated measurements of the red UC emission spectra at room temperature is approximately 0.012%. Fig. 3(d) displays the fitted curve of δT for the FIR_R optical thermometer, in which the values gradually increase with rising temperature, achieving a minimum of 0.025 K at 298 K. Notably, δT remains below 0.1 K throughout the entire tested temperature range, indicating the excellent optical thermometric performance of the FIR_R-based optical thermometer.

As shown in Fig. 4(a), the temperature dependence of the $^4I_{11/2} \rightarrow {}^4I_{15/2}$ transition is tested and normalized at 1028 nm. The Stark splittings at 985 nm and 1028 nm are selected for FIR-based optical thermometry. The fitting curve between FIR_N and the temperature is presented in Fig. 4(b), with the corresponding fitting equation expressed as

$$FIR_N = I_{985}/I_{1028} = \exp(160.1/T), \quad (8)$$

from which the ΔE value is calculated to be 111 cm^{-1}. Based on the relationship of FIR_N and temperature, the fitting curves for S_A and S_R of FIR_N are calculated and shown in Fig. 4(c). At 298 K, the values of S_A and S_R are 0.32% K^{-1} and 0.18% K^{-1}, respectively, after which both parameters decrease with increasing temperature. According to the δFIR/FIR value (0.122%) obtained from 50 repeated measurements of the NIR emission spectra at room temperature (see Fig. S2(b)), the δT curve of the FIR_N optical thermometer is fitted and shown in Fig. 4(d), which exhibits an increasing trend with rising temperature along with a minimum value of 0.68 K at the beginning temperature.

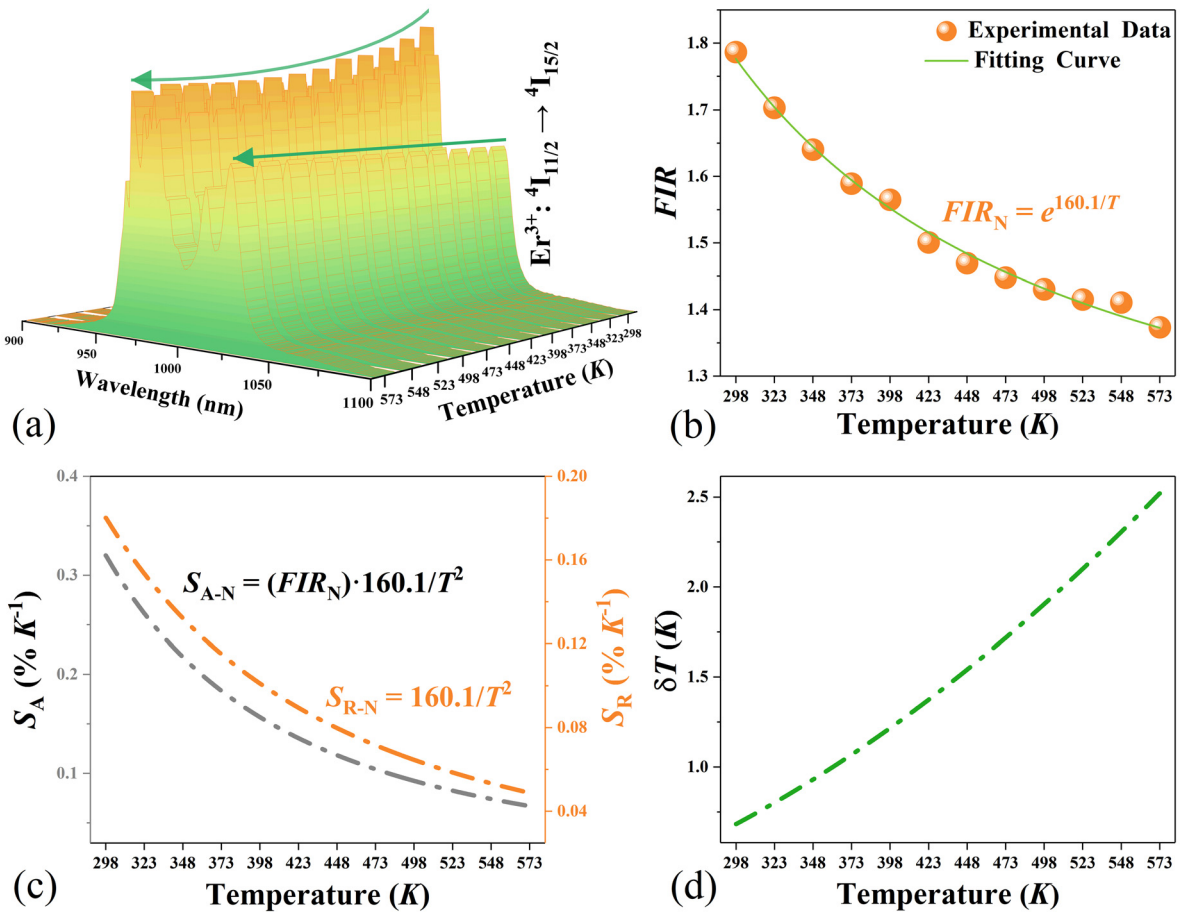

Fig. 4 Temperature dependence of (a) the $^4I_{11/2} \rightarrow {}^4I_{15/2}$ transition along with the corresponding (b) FIR, (c) S_A and S_R and (d) δT.

Table 1 Typical optical thermometers based on the FIR of Stark sublevels and their critical parameters

Host	Dopants	EX (nm)	Transition	Working range (K)	$S_{A\text{-max}}$ (% K^{-1})	$S_{R\text{-max}}$ (% K^{-1})	Ref.
$CaSc_2O_4$	Er^{3+}/Ho^{3+}	1532	Er^{3+}:$^4F_{9/2} \rightarrow {}^4I_{15/2}$	298–573	0.26	0.48	This work
$CaSc_2O_4$	Er^{3+}/Ho^{3+}	1532	Er^{3+}:$^4I_{11/2} \rightarrow {}^4I_{15/2}$	298–573	0.32	0.18	This work
YVO_4	Nd^{3+}	808	Nd^{3+}:$^4F_{3/2} \rightarrow {}^4I_{11/2}$	298–333	—	0.25	33
$BaMoO_4$	Yb^{3+}/Er^{3+}	980	Er^{3+}:$^4I_{13/2} \rightarrow {}^4I_{15/2}$	293–573	0.065	0.129	34
TiO_2	$Yb^{3+}/Er^{3+}/Mo^{6+}$	976	Er^{3+}:$^2H_{11/2} \rightarrow {}^4I_{15/2}$	307–673	—	0.132	35
TiO_2	$Yb^{3+}/Er^{3+}/Mo^{6+}$	976	Er^{3+}:$^4S_{3/2} \rightarrow {}^4I_{15/2}$	307–673	—	0.136	35
TiO_2	$Yb^{3+}/Er^{3+}/Mo^{6+}$	976	Er^{3+}:$^4F_{9/2} \rightarrow {}^4I_{15/2}$	307–673	—	0.114	35
CaF_2	Nd^{3+}/Y^{3+}	980	Nd^{3+}:$^4F_{3/2} \rightarrow {}^4I_{11/2}$	300–335	—	0.113	36

Table 1 summarizes a series of typical optical thermometers based on the FIR technique utilizing Stark sublevels along with their corresponding excitation wavelength, operating temperature range, and maximum S_A and S_R. Distinctly, the optical thermometer $CaSc_2O_4$:Er^{3+}/Ho^{3+} in this study is the only one with an excitation wavelength within the NIR-II region, and it exhibits the highest S_A and S_R values as well as a wide temperature measurement range, suggesting its significant potential for temperature sensing, especially in the biomedicine field.

A simple *in vitro* experiment is designed at room temperature to evaluate the detection depth of the sample within biological tissues. As illustrated in Fig. 5(a) and (b), the emission intensity of red and NIR luminescence gradually decreases with the increasing thickness of fresh chicken muscle tissues, which is attributed to the absorption and scattering effects of the biological tissues. Despite this attenuation, the spectral signals corresponding to $^4F_{9/2} \rightarrow {}^4I_{15/2}$ and $^4I_{11/2} \rightarrow {}^4I_{15/2}$ transitions remain detectable at tissue depths of 6 mm and 8 mm, respectively. Furthermore, as shown in Fig. 5(c), the values of

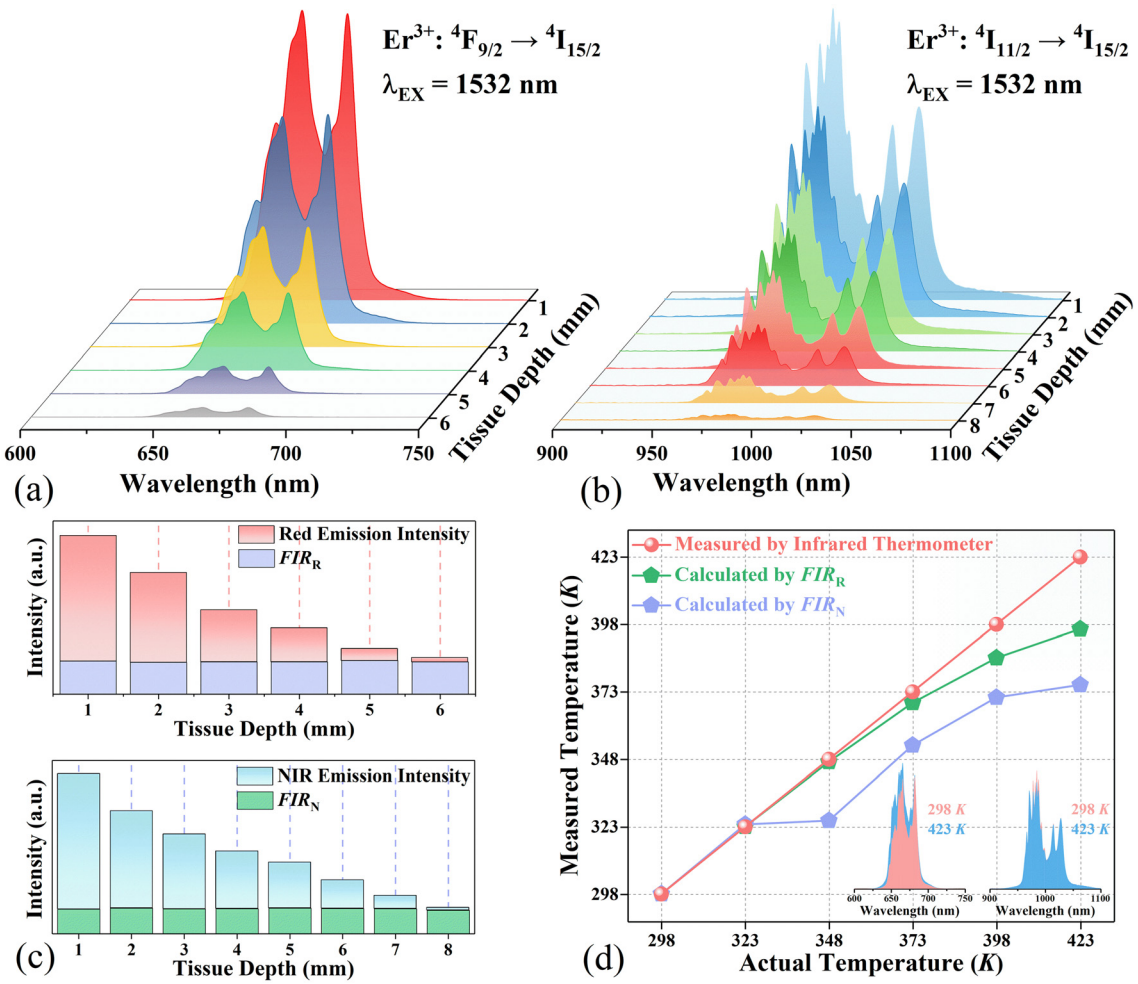

Fig. 5 Emission spectra of (a) red and (b) NIR light and (c) the emission intensities and FIR values as a function of the biological tissue thickness. (d) Sample temperature detected by FIR_R, FIR_N and infrared thermometers; insets show the normalized emission spectra measured at 298 K and 423 K.

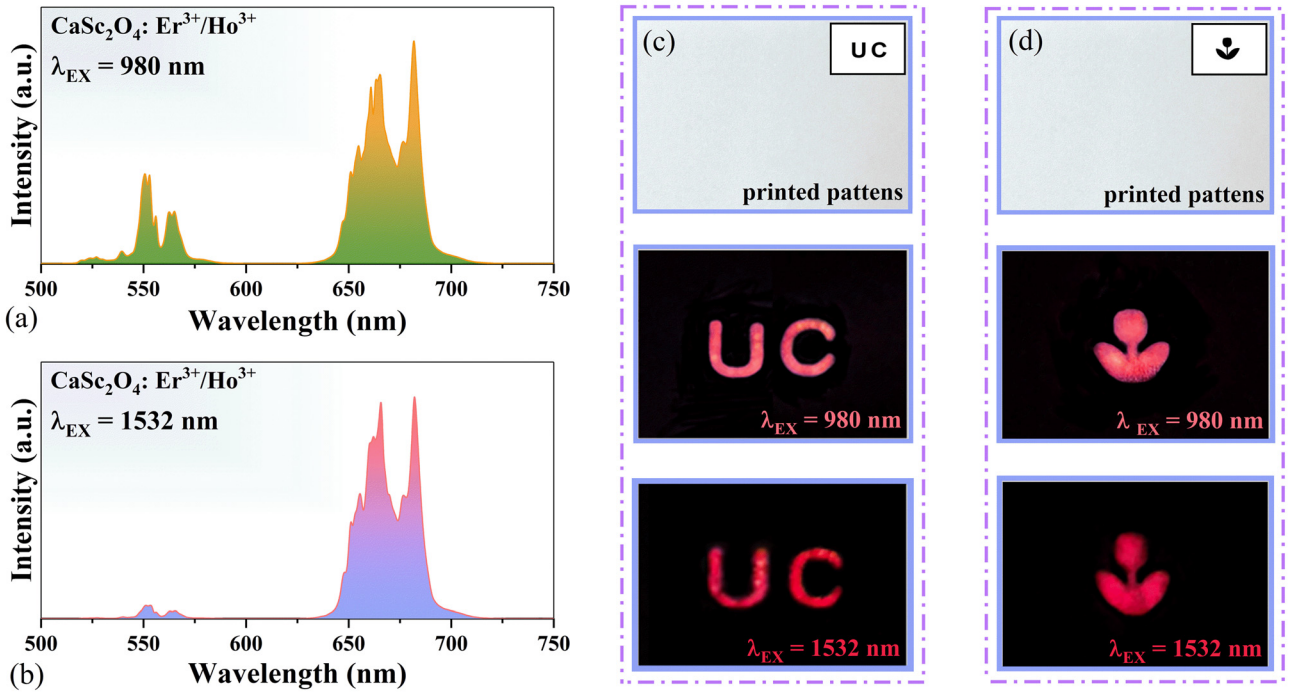

Fig. 6 UC spectrum of the sample excited at (a) a 980 nm wavelength and (b) a 1532 nm wavelength. Photographs of the pattern (c) "UC" and (d) "flower" under various illumination conditions.

FIR_R and FIR_N remain nearly constant with increasing tissue thickness, demonstrating their significant potential for temperature sensing in deep biological tissues. Concurrently, the sample is heated using a heat gun while its temperature is simultaneously monitored using an infrared thermometer and the FIR thermometric technique. As shown in Fig. 5(d), the temperature values measured by FIR_R and FIR_N align well with the standard temperature values obtained from the infrared thermometer, further validating their superior optical thermometric performance. Additionally, Fig. S3 presents the reproducibility study of FIR_R and FIR_N over thermal cycling between 298 K and 573 K, which remain nearly constant throughout the cycling process, demonstrating the excellent reproducibility and reliability of the sample.

Anti-counterfeiting application

In addition to being excited by a 1532 nm wavelength, the as-prepared $CaSc_2O_4$:Er^{3+}/Ho^{3+} powder can also be excited by a 980 nm wavelength. More importantly, the sample exhibits a certain difference in the red-to-green ratio and the emission color under the excitation of the two wavelengths due to the distinct variation in the ET mechanism (Fig. S4), as shown in Fig. 6(a) and (b). This property endows the material with potential applications in optical anti-counterfeiting. Therefore, a fluorescent colloid is prepared by mixing ethanol and polydimethylsiloxane (PDMS) in a 1 : 1 volume ratio, followed by incorporation of 5 wt% $CaSc_2O_4$:Er^{3+}/Ho^{3+} powder. Subsequently, two drops of the curing agent are added and mixed uniformly to obtain the fluorescent ink, which is utilized for screen-printing "UC" lettering and floral patterns. As shown in Fig. 6(c) and (d), the printed patterns remain invisible under daylight conditions. However, the faint red patterns emerge on the papers upon irradiation with 980 nm light, while 1532 nm excitation induces a transition to a deep red hue. The above research confirms that this material can substantially enhance the concealment and security performance of optical anti-counterfeiting technology.

Conclusions

In summary, 1532 nm-driven nearly pure red UC luminescence is realized in $CaSc_2O_4$:Er^{3+} through Ho^{3+} doping, achieving an approximately 19-fold improvement in the red-to-green ratio compared to the Ho^{3+}-free sample. Spectroscopic analysis reveals that the dramatic improvement of emission color purity primarily originates from the modification of ET pathways induced by Ho^{3+} doping. Leveraging the Stark splitting of $^4F_{9/2} \rightarrow {}^4I_{15/2}$ and $^4I_{11/2} \rightarrow {}^4I_{15/2}$ transitions, highly sensitive optical thermometers FIR_R and FIR_N are developed, exhibiting maximum S_R of 0.48% K^{-1} and 0.18% K^{-1} for temperature detection, respectively. Beyond that, *in vitro* experiments demonstrate that FIR_R and FIR_N enable penetration depths of 6 mm and 8 mm in biological tissues while maintaining largely unaffected FIR values. Meanwhile, a tunable emission color from faint red to deep red is achieved by varying the excitation wavelength from 980 nm to 1532 nm, which imparts the powder with high concealment and security for optical anti-

counterfeiting applications. All of these findings validate that the red UC luminescent material $CaSc_2O_4$:Er^{3+}/Ho^{3+} with high color purity not only enables high-sensitivity optical temperature sensing in deep biological tissues but also holds potential for optical anti-counterfeiting applications.

Conflicts of interest

There are no conficts to declare.

Data availability

The data used to support the findings of this study are available from the corresponding author upon request.

Supplementary information (SI) is available. See DOI: https://doi.org/10.1039/d5dt01973g.

Acknowledgements

This work is financially supported by the National Natural Science Foundation of China (11704054), the Natural Science Foundation of Chongqing (CSTB2025NSCQ-GPX1264, CSTB2025NSCQ-GPX1290, CSTB2025NSCQ-LZX0080, and CSTB2024NSCQ-LZX0030) and the Science and Technology Research Program of Chongqing Municipal Education Commission (KJZD-M202500602, KJZD-K20250060, KJZD-M202300601, and KJQN202100639).

References

1 A. Chu, H. He, Z. Yin, R. Peng, H. Yang, X. Gao, D. Luo, R. Chen, G. Xing and Y. Liu, Plasmonically enhanced upconversion luminescence via holographically formed silver nanogratings, *ACS Appl. Mater. Interfaces*, 2019, **12**, 1292–1298.

2 Z. Cai, Z. An, H. Huang, Y. Zhao and B. Zhou, High-sensitive nonthermally coupled upconversion for ultralow temperature sensing, *J. Rare Earths*, 2024, **42**, 2027–2032.

3 G. Xiang, X. Liu, Q. Xiao, X. Liu, S. Xu, S. Jiang, X. Zhou, L. Li, D. Wu, L. Ma, X. Wang and J. Zhang, Design of a bifunctional $NaScF_4$: Yb^{3+}/Er^{3+} nanoparticles for deep-tissue bioimaging and optical thermometry through Mn^{2+} doping, *Talanta*, 2021, **224**, 121832.

4 Y. Cha, B. Seo, M. Chung, B. S. Kim, W. Choi and W. Park, Skin-inspired thermometer enabling contact-independent temperature sensation via a seebeck-resistive bimodal system, *ACS Appl. Mater. Interfaces*, 2022, **14**, 17920–17926.

5 A. A. Lyapin, A. S. Ermakov, S. V. Kuznetsov, S. V. Gushchin, P. A. Ryabochkina, V. A. Konyushkin, A. N. Nakladov and P. P. Fedorov, Upconversion luminescence of CaF2-SrF2-ErF3 single crystals upon 1.5 μm laser excitation, *J. Phys.:Conf. Ser.*, 2019, **1410**, 012086.

6 X. Zheng, R. K. Kankala, C. G. Liu, S. B. Wang, A. Z. Chen and Y. Zhang, Lanthanides-doped near-infrared active upconversion nanocrystals: Upconversion mechanisms and synthesis, *Coord. Chem. Rev.*, 2021, **438**, 213870.

7 C. Sun, B. Li, M. Zhao, S. Wang, Z. Lei, L. Lu, H. Zhang, L. Feng, C. Dou, D. Yin and H. Xu, J-aggregates of cyanine dye for NIR-II in vivo dynamic vascular imaging beyond 1500 nm, *J. Am. Chem. Soc.*, 2019, **141**, 19221–19225.

8 S. Liu, L. Yan, J. Huang, Q. Zhang and B. Zhou, Controlling upconversion in emerging multilayer core-shell nanostructures: from fundamentals to frontier applications, *Chem. Soc. Rev.*, 2022, **51**, 1729–1765.

9 Q. Chen, X. Xie, B. Huang, L. Liang, S. Han, Z. Yi, Y. Wang, Y. Li, D. Fan, L. Huang and X. Liu, Confining excitation energy in Er^{3+}-sensitized upconversion nanocrystals through Tm^{3+}-mediated transient energy trapping, *Angew. Chem.*, 2017, **129**, 7713–7717.

10 A. L. Antaris, H. Chen, K. Cheng, Y. Sun, G. Hong, C. Qu, S. Diao, Z. Deng, X. Hu, B. Zhang and X. Zhang, A small-molecule dye for NIR-II imaging, *Nat. Mater.*, 2016, **15**, 235–242.

11 H. Wang, Y. Xu, T. Pang, B. Chen, F. Xin, M. Xing, M. Tian, Y. Fu, X. Luo and Y. Tian, Engineering E^{r3+}-sensitized nanocrystals to enhance NIR II-responsive upconversion luminescence, *Nanoscale*, 2022, **14**, 962–968.

12 W. Zhou, J. Yang, X. L. Jin, Y. Peng and J. Luo, A 1532 nm laser-excited upconversion luminescent $NaLuF_4$: Er microcrystals for optical thermometers, *Chem. Phys. Lett.*, 2023, **810**, 140198.

13 T. Castro, D. Manzani and S. J. L. Ribeiro, Up-conversion mechanisms in Er^{3+}-doped fluoroindate glasses under 1550 nm excitation for enhancing photocurrent of crystalline silicon solar cell, *J. Lumin.*, 2018, **200**, 260–264.

14 X. Liu, T. Liu, L. Tu, J. Zuo, J. Li, Y. Feng and C. J. Yao, Enhancing NIR-II Upconversion Monochromatic Emission for Temperature Sensing, *Small*, 2024, **20**, 2308748.

15 T. Sun, Y. Li, W. L. Ho, Q. Zhu, X. Chen, L. Jin, H. Zhu, B. Huang, J. Lin, B. E. Little and S. T. Chu, Integrating temporal and spatial control of electronic transitions for bright multiphoton upconversion, *Nat. Commun.*, 2019, **10**, 1811.

16 X. Yin, W. Xu, G. Zhu, Y. Ji, Q. Xiao, X. Dong, M. He, B. Cao, N. Zhou, X. Luo, L. Guo and D. Bin, Towards highly efficient NIR II response up-conversion phosphor enabled by long lifetimes of Er^{3+}, *Nat. Commun.*, 2022, **13**, 6549.

17 H. Lin, D. Xu, Y. Li, L. Yao, L. Xu, Y. Ma, S. Yang and Y. Zhang, Intense red upconversion luminescence in Er^{3+}-sensitized particles through confining the 1532 nm excitation energy, *J. Lumin.*, 2019, **216**, 116731.

18 D. Przybylska and T. Grzyb, Synthesis and up-conversion of core/shell SrF_2: Yb^{3+}, Er^{3+}@ SrF_2: Yb^{3+}, Nd^{3+} nanoparticles under 808, 975, and 1532 nm excitation wavelengths, *J. Alloys Compd.*, 2020, **831**, 154797.

19 H. Wu, Z. Hao, L. Zhang, X. Zhang, G. H. Pan, Y. Luo, H. Wu, H. Zhao, H. Zhang and J. Zhang, Enhancing IR to NIR upconversion emission in Er^{3+}-sensitized phosphors by adding Yb^{3+} as a highly efficient NIR-emitting center for

photovoltaic applications, *CrystEngComm*, 2020, **22**, 229–236.

20 W. Zhou, J. Yang and X. Jin, Red light intensity modulation, temperature sensing and bioimaging of $NaLuF_4$: Er^{3+}/Tm^{3+}/Yb^{3+} microcrystals under 1532 nm laser excitation, *J. Alloys Compd.*, 2024, **979**, 173534.

21 S. J. Budijono, J. Shan, N. Yao, Y. Miura, T. Hoye, R. H. Austin, Y. Ju and R. K. Prud'homme, Synthesis of stable block-copolymer-protected $NaYF_4$: Yb^{3+}, Er^{3+} up-converting phosphor nanoparticles, *Chem. Mater.*, 2010, **22**, 311–318.

22 L. Xu, J. Liu, L. Pei, Y. Xu and Z. Xia, Enhanced up-conversion luminescence and optical temperature sensing in graphitic C_3N_4 quantum dots grafted with $BaWO_4$: Yb^{3+}, Er^{3+} phosphors, *J. Mater. Chem. C*, 2019, **7**, 6112–6119.

23 G. Xiang, X. Liu, Q. Xia, S. Jiang, X. Zhou, L. Li, Y. Jin, L. Ma, X. Wang and J. Zhang, Deep-tissue temperature sensing realized in BaY_2O_4: Yb^{3+}/Er^{3+} with ultrahigh sensitivity and extremely intense red upconversion luminescence, *Inorg. Chem.*, 2020, **59**, 11054–11060.

24 X. Luo, Q. Chen, H. Guo, H. Zhang, X. He and W. Zhao, One-step hydrothermal synthesis of Cit-$NaYbF_4$: Er^{3+} nanocrystals with enhanced red upconversion emission for in vivo fluorescence molecular tomography, *J. Rare Earths*, 2024, **42**, 36–45.

25 S. Ding, L. Lu, Y. Fan and F. Zhang, Recent progress in NIR-II emitting lanthanide-based nanoparticles and their biological applications, *J. Rare Earths*, 2020, **38**, 451–463.

26 Y. Qiao, S. Qiao, X. Yu, Q. Min, C. Pi, J. Qiu, H. Ma, J. Yi, Q. Zhan and X. Xu, Plant tissue imaging with bipyramidal upconversion nanocrystals by introducing Tm^{3+} ions as energy trapping centers, *Nanoscale*, 2021, **13**, 8181–8187.

27 H. Chen, B. Ding, P. A. Ma and J. Lin, Recent progress in upconversion nanomaterials for emerging optical biological applications, *Adv. Drug Delivery Rev.*, 2022, **188**, 114414.

28 E. M. Chan, G. Han, J. D. Goldberg, D. J. Gargas, A. D. Ostrowski, P. J. Schuck, B. E. Cohen and D. J. Milliron, Combinatorial discovery of lanthanide-doped nanocrystals with spectrally pure upconverted emission, *Nano Lett.*, 2012, **12**, 3839–3845.

29 L. Liu, S. Wang, B. Zhao, P. Pei, Y. Fan, X. Li and F. Zhang, Er^{3+} Sensitized 1530 nm to 1180 nm second near-infrared window upconversion nanocrystals for in vivo biosensing, *Angew. Chem.*, 2018, **130**, 7640–7644.

30 S. Bi, Z. Deng, J. Huang, X. Wen and S. Zeng, NIR-II responsive upconversion nanoprobe with simultaneously enhanced single-band red luminescence and phase/size control for bioimaging and photodynamic therapy, *Adv. Mater.*, 2023, **35**, 2207038.

31 H. Wu, Z. Hao, L. Zhang, X. Zhang, Y. Xiao, G. H. Pan, H. Wu, Y. Luo, L. Zhang and J. Zhang, Er^{3+}/Yb^{3+} codoped phosphor $Ba_3Y_4O_9$ with intense red upconversion emission and optical temperature sensing behavior, *J. Mater. Chem. C*, 2018, **6**, 3459–3467.

32 Y. Liu, B. Duan, L. Zhou, Y. Wu, F. Wang, C. Ding and J. Hu, Large enhancement of red upconversion luminescence in beta $Ba_2Sc_{0.67}Yb_{0.3}Er_{0.03}AlO_5$ phosphor via Mn^{2+} ions doping for thermometry, *Sci. Rep.*, 2024, **14**, 8893.

33 I. E. Kolesnikov, E. V. Golyeva, A. A. Kalinichev, M. A. Kurochkin, E. Lähderanta and M. D. Mikhailov, Nd^{3+} single doped YVO_4 nanoparticles for sub-tissue heating and thermal sensing in the second biological window, *Sens. Actuators, B*, 2017, **243**, 338–345.

34 R. Lei, X. Liu, F. Huang, D. Deng, S. Zhao, H. Xu and S. Xu, Optical thermometry based on anomalous temperature-dependent 1.53 μm infrared luminescence of Er^{3+} in $BaMoO_4$: Er^{3+}/Yb^{3+} phosphor, *Opt. Mater.*, 2018, **86**, 278–285.

35 B. Cao, J. Wu, X. Wang, Y. He, Z. Feng and B. Dong, Multiple temperature-sensing behavior of green and red upconversion emissions from Stark sublevels of Er^{3+}, *Sensors*, 2015, **15**, 30981–30990.

36 M. Quintanilla, Y. Zhang and L. M. Liz-Marzan, Subtissue plasmonic heating monitored with CaF_2: Nd^{3+}, Y^{3+} nanothermometers in the second biological window, *Chem. Mater.*, 2018, **30**, 2819–2828.